φ production in In–In collisions at 158 A GeV

The NA60 Collaboration

R. Arnaldi[12], **K. Banicz**[5,7], **K. Borer**[1], **J. Castor**[6], **B. Chaurand**[9], **W. Chen**[2], **C. Cicalò**[4], **A. Colla**[11,12], **P. Cortese**[11,12], **S. Damjanovic**[5,7], **A. David**[5,8], **A. de Falco**[3,4], **A. Devaux**[6], **L. Ducroux**[13], **H. En'yo**[10], **J. Fargeix**[6], **A. Ferretti**[11,12], **M. Floris**[3,4,a], **A. Förster**[5], **P. Force**[6], **N. Guettet**[5,6], **A. Guichard**[13], **H. Gulkanyan**[14], **J. Heuser**[10], **M. Keil**[5,8], **L. Kluberg**[5,9], **Z. Li**[2], **C. Lourenço**[5], **J. Lozano**[8], **F. Manso**[6], **P. Martins**[5,8], **A. Masoni**[4], **A. Neves**[8], **H. Ohnishi**[10], **C. Oppedisano**[12], **P. Parracho**[5,8], **P. Pillot**[13], **T. Poghosyan**[14], **G. Puddu**[3,4], **E. Radermacher**[5], **P. Ramalhete**[5,8], **P. Rosinsky**[5], **E. Scomparin**[12], **J. Seixas**[8], **S. Serci**[3,4], **R. Shahoyan**[5,8], **P. Sonderegger**[8], **H.J. Specht**[7], **R. Tieulent**[13], **A. Uras**[3,4], **G. Usai**[3,4], **R. Veenhof**[5,15], **H.K. Wöhri**[4,8]

[1]Laboratory for High Energy Physics, Bern, Switzerland
[2]BNL, Upton, NY, USA
[3]Università di Cagliari, Cagliari, Italy
[4]INFN Cagliari, Cagliari, Italy
[5]CERN, Geneva, Switzerland
[6]Université Blaise Pascal and CNRS-IN2P3, Clermont-Ferrand, France
[7]Physikalisches Institut der Universität Heidelberg, Heidelberg, Germany
[8]Istituto Superior Técnico, Lisbon, Portugal
[9]LLR, Ecole Polytechnique and CNRS-IN2P3, Palaiseau, France
[10]RIKEN, Wako, Saitama, Japan
[11]Università di Torino, Torino, Italy
[12]INFN Torino, Torino, Italy
[13]IPNL, Université de Lyon, Université Lyon 1, CNRS/IN2P3, Villeurbanne, France
[14]YerPhI, Yerevan Physics Institute, Yerevan, Armenia
[15]University of Wisconsin, Milwaukee, USA

Abstract The NA60 experiment has measured muon pair production in In–In collisions at 158 AGeV at the CERN SPS. This paper presents a high statistics measurement of $\phi \rightarrow \mu\mu$ meson production. Differential spectra, yields, mass and width are measured as a function of centrality and compared to previous measurements in other colliding systems at the same energy. The width of the rapidity distribution is found to be constant as a function of centrality, compatible with previous results. The decay muon polar angle distribution is measured in several reference frames. No evidence of polarization is found as a function of transverse momentum and centrality. The analysis of the p_T spectra shows that the ϕ has a small radial flow, implying a weak coupling to the medium. The T_{eff} parameter measured in In–In collisions suggests that the high value observed in Pb–Pb in the kaon channel is difficult to reconcile with radial flow alone. The absolute yield is compared to results in Pb–Pb collisions: though significantly smaller than measured by NA50 in the muon channel, it is found to exceed the NA49 and CERES data in the kaon channel at any centrality. The mass and width are found to be compatible with the PDG values at any centrality and at any p_T: no evidence for in-medium modifications is observed.

1 Introduction

QCD predicts the occurrence of a phase transition from hadronic matter to a deconfined plasma of quarks and gluons, when sufficiently high energy densities are reached. Strangeness enhancement was proposed long ago as a signature of this phase transition [1, 2]. The ϕ meson is a key experimental probe in this context: due to its $s\bar{s}$ valence quark content it permits to measure strangeness production. It was suggested that, being a hidden strangeness state, the ϕ should not be sensitive to canonical suppression, and can thus be used to test strangeness enhancement models [3–7].

a e-mail: michele.floris@ca.infn.it

2

Eur. Phys. J. C (2009) 64: 1–18

Moreover, it has been argued that the spectral function of the ϕ or of its decay products could be modified in the medium. This would reflect in changes of its mass and partial decay widths. Mass shifts of vector mesons, as a consequence of the change of the quark condensate in the medium, were originally proposed by Brown and Rho [8]. Subsequently, the ϕ meson mass dependence on the medium density was calculated with QCD sum rules [9]. Modifications of the width in the context of this dropping mass scenario were investigated, for instance, in the model of Ref. [10]. As an alternative approach, both the mass and width changes were studied in the framework of hadronic many body models (see [11] for an up-to-date discussion), which predict a broadening and no or small mass shift. Finally, it was suggested that in-medium changes could also appear in cold nuclear matter [12, 13].

It is important to point out that, contrary to the ρ meson, which has a lifetime of 1.3 fm, much smaller than the lifetime of the fireball (7–10 fm), the ϕ has a lifetime of 44 fm. Therefore in-medium effects on the mass or width might be difficult to isolate experimentally, and might only appear at very low p_T. A possible way of tracing down those modifications is the comparison of the particle yields and spectra in the dilepton and in the kaon channel: since the ϕ is almost at the threshold for the $\phi \to K\bar{K}$ channel, even a small change in its spectral properties should lead to a significant difference in the two channels [14]. A discrepancy in the two channels could also be ascribed to final state effects related to in-medium kaon absorption or rescattering [15, 16].

The KEK-PS E325 experiment reported evidence for a large excess to the low mass side of ϕ peak in p-Cu at 12 GeV for $\beta\gamma < 1.25$, corresponding to slow ϕ mesons, having a higher chance to decay inside the Cu nucleus (the effect was not observed in p-C and for higher values of $\beta\gamma$) [17]. This excess was explained in terms of an in-medium modified component with mass decreased by $\sim$35 MeV and width broadened by a factor 3.6 with respect to the PDG value. The reported yield associated to this excess is very significant: 20% of the total ϕ yield.

ϕ production was studied extensively at the SPS by several experiments. NA49 measured ϕ production in p–p, C–C, Si–Si and Pb–Pb at 158 AGeV in the $\phi \to K^+K^-$ channel [18–20]. These data show that the ϕ yield breaks N_{part} scaling and that the ϕ enhancement, quantified as $\langle\phi\rangle/N_{part}$, saturates already for Si–Si central collisions. Pb–Pb collisions were also studied in different experimental conditions by the NA50 experiment, which found contrasting results. NA50 studied the $\phi \to \mu\mu$ channel [21] with acceptance limited to $p_T > 1.1$ GeV, while the NA49 measurement in the $\phi \to K^+K^-$ channel was limited to $p_T < 1.6$ GeV because of statistics. Both experiments observed an enhancement of the ϕ yield with the size of the collision system. The absolute yields, however, disagree by a factor $\sim$4 in full

phase space [22]. A recent NA50 analysis of a new sample confirmed previous findings [23]. The NA49 and NA50 results disagree also on the T_{eff} parameters extracted from the transverse mass spectra fitted with the thermal ansatz. The NA49 T_{eff} values are consistently larger and show a stronger centrality dependence than those measured by NA50. While this could be partly due to the radial expansion, which flattens the distributions at low m_T, the effect is too large to be explained by radial flow alone.

Naively, kaon absorption or rescattering could prevent the reconstruction of in-matter $\phi \to K\bar{K}$ decays, in particular at low transverse momentum, while the ϕ mesons decaying in the lepton channel would not be affected. This would lead to reduced yields and enhanced T_{eff} in the $K\bar{K}$ channel as compared to the $\mu\mu$ channel. Meson modification in the medium could also lead to differences in the two channels, as mentioned above. The difference between NA49 and NA50, however, is larger than predicted by models including all these effects [10, 14–16, 24]. The discrepancies in absolute yields and T_{eff} became known as the ϕ puzzle.

Production of ϕ in central Pb–Pb collisions was recently studied also by CERES [25] both in the kaon and dielectron channels. The measured T_{eff} and yield are compatible with the NA49 results. However, due to the large uncertainty in the dielectron channel, the authors could not rule out completely a possible difference in the two channels, though significantly smaller than the NA49/NA50 difference: the maximum possible enhancement in the leptonic over hadronic channel was estimated to be 1.6 at 95% confidence level.

In this paper we report on new measurements in the muon channel done by the NA60 collaboration in In–In collisions at 158 AGeV incident beam energy, which can help to clarify ϕ production in nuclear collisions. Transverse momentum and yields have been studied as a function of centrality. Transverse momentum spectra, measured in the range 0–3 GeV, and yields are compared to previous results, providing further insight on the ϕ puzzle. The mass and width of the ϕ are studied as a function of centrality and p_T, in order to search for possible in-medium effects. The results are compared to previous measurements and existing theoretical predictions for In–In collisions. In addition, the rapidity and the decay angular distributions in three reference frames (Collins–Soper, Gottfried–Jackson and the helicity frame) are also measured. In elementary collisions, the ϕ decay angular distributions can convey information on the production mechanism [26]. No measurements exist in p–p, while the ACCMOR collaboration performed measurements of the ϕ polarization in pion–, proton– and kaon–Be interactions [27, 28]. A small but significant transverse polarization was reported at low p_T in the Gottfried–Jackson frame, which was related to the parton fusion model to estimate the average mass of the fusing partons. More recently, NA60 measured the angular distributions in In–In collisions,

integrated in centrality and for $p_T > 0.6$ GeV, for the excess dimuons below 1 GeV (dominated by $\pi^+\pi^- \to \rho \to \mu^+\mu^-$) and the vector mesons ω and ϕ [29]. The reported absence of any anisotropy indicates the completely random orientation of the interacting hadrons in 3 dimensions as expected in the case of a thermalized medium. In this paper we extend these results by performing the study as a function of centrality and p_T.

2 The NA60 apparatus

In this section the detectors of the NA60 apparatus used in the analysis are briefly described. A more detailed description can be found in Ref. [30].

The 17-m-long muon spectrometer, previously used by the NA38 and NA50 experiments [31], is complemented by new silicon detectors in the vertex region. The experimental apparatus is shown in Fig. 1. The muon spectrometer is composed of 8 multi-wire proportional chambers and 4 scintillator trigger hodoscopes, divided into a "forward" and a "backward" telescope by the 5-m-long ACM (Air Core Magnet) toroidal magnet. A 120 cm thick iron wall, located just before the last trigger hodoscope and after the tracking chambers, ensures that only muons can trigger the apparatus, without degradation of the tracking accuracy. The angular acceptance is $35 < \theta < 120$ mrad; the rapidity coverage for the ϕ is $3 \lesssim y \lesssim 4.2$.

A 12 λ_i hadron absorber, mostly made of graphite, is placed in front of the tracking system of the muon spectrometer, as close as possible to the target to minimize the fraction of hadrons that decay into muons. The identification provided by this "muon filter" leads to a very selective trigger, enabling the experiment to run at very high luminosities. However, the material in the hadron absorber also degrades the kinematics of the muons, because of energy loss fluctuations and multiple scattering. This affects in particular the angular resolution, which is ~10 mrad for typical muons from ϕ decays.

The layout of the vertex region is shown schematically in Fig. 2. Downstream of the target and before the hadron absorber, a silicon tracking telescope [32] embedded inside a 2.5 T magnetic dipole field measures the charged tracks produced in the interaction. The muons in the vertex region are then identified by matching them to the tracks reconstructed in the muon spectrometer. As described in the next section, this significantly improves the performance of the detector. The telescope used during the indium run consisted of 16 independent detector planes, providing 11 tracking points, arranged along the beam axis over a length of ~26 cm, starting at ~7 cm from the target center. The telescope covers the angular acceptance of the muon spectrometer, with the first planes smaller than the last ones. Each plane consists of several single-chip pixel detector assemblies, 96 in total, which are mounted on a planar ceramic support. The assemblies
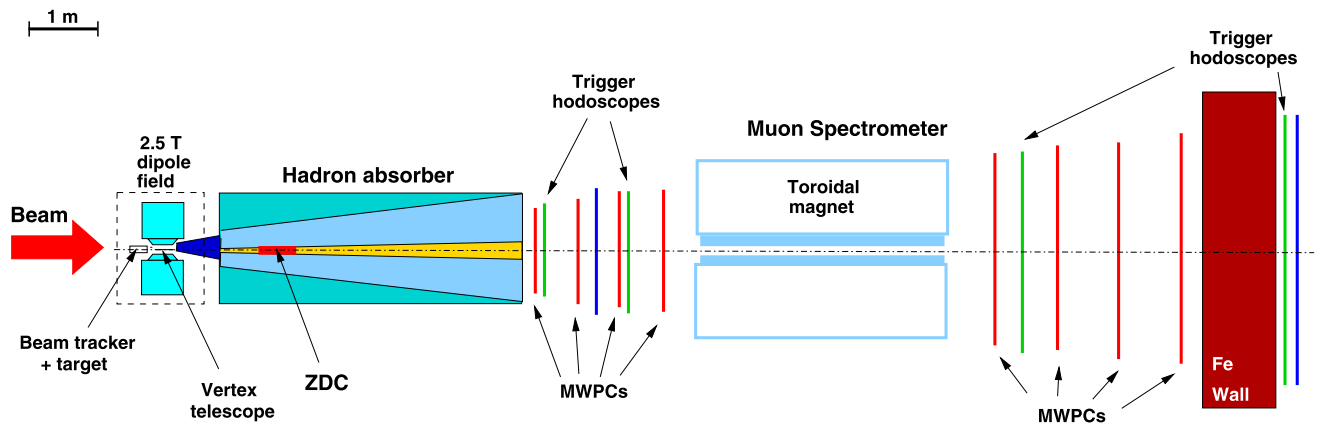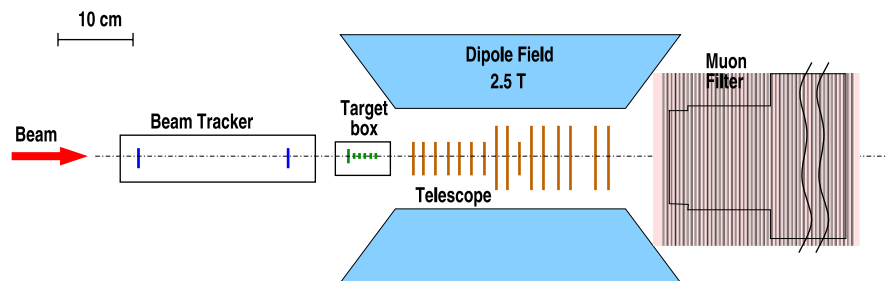

Fig. 1 The NA60 experimental apparatus

Fig. 2 Detail of the vertex detectors layout

are made of radiation tolerant, 750 μm thick ALICE1LHCb pixel readout chips [33], bump-bonded to 300 μm thick p-on-n silicon pixel sensors, with 425×50 μm^2 pixels. Each of the single-chip assemblies is a matrix of 32 columns and 256 rows. They have been shown to remain fully functional up to a radiation dose of 12 Mrad [34]. The detector coped well with the radiation level of ~1 Mrad per week, reached in the cells around the beam axis of the first planes in the NA60 environment [35]. The telescope tracks all charged particles produced in the collision, thus providing an estimate of the collision centrality.

Incoming ions are tracked by a silicon microstrip beam tracker, composed of two stations placed 20 cm apart (30 cm and 10 cm upstream of the target). The 400 μm thick sensors have 24 strips of 50 μm pitch, allowing to infer the transverse coordinates of the interaction point, at the target, with a resolution of 20 μm [36]. They are operated at cryogenic temperatures (130 K), to remain sensitive to the beam ions even after collecting considerable radiation doses [37]. The "back planes" of the four sensors extend over a larger area and constitute a very good beam intensity counter.

Embedded inside the hadron absorber, a Zero Degree Calorimeter (ZDC) provides an alternative estimate of the collision centrality by measuring the energy carried by the projectile nucleons which have not taken part in the interaction (spectators) [38, 39]. The ZDC and the beam tracker were used to measure the beam intensity in the absolute yield measurement (Sect. 4.4).

3 Data sample and analysis procedure

During the 5-week-long run in 2003, 230 million muon pair (*dimuon*) triggers were recorded, with two different settings of the ACM magnet current (4000 A and 6500 A). The results presented in this paper refer to the 4000 A data sample, which amounts to ~50% of the total statistics, as the 6500 A setting suppresses the low mass acceptance and it is optimal for the study of the J/ψ.

The data were collected with a 158 A GeV indium beam, incident on 7 indium targets of 17% total interaction probability. The targets were placed in vacuum in order not to pollute the data sample with In-air interactions. The z coordinate of the interaction vertex is shown in Fig. 3. The resolution on the position of the interaction vertex is 10–20 μm in the transverse coordinates and ~200 μm in the longitudinal coordinate. The target identification is extremely good, with negligible background between different targets. Other elements present along the beam line are also clearly visible in the picture, like the target box windows and the beam tracker stations.

In the following subsections we illustrate briefly the most relevant aspects of the reconstruction and selection of events, background subtraction and acceptance correction.
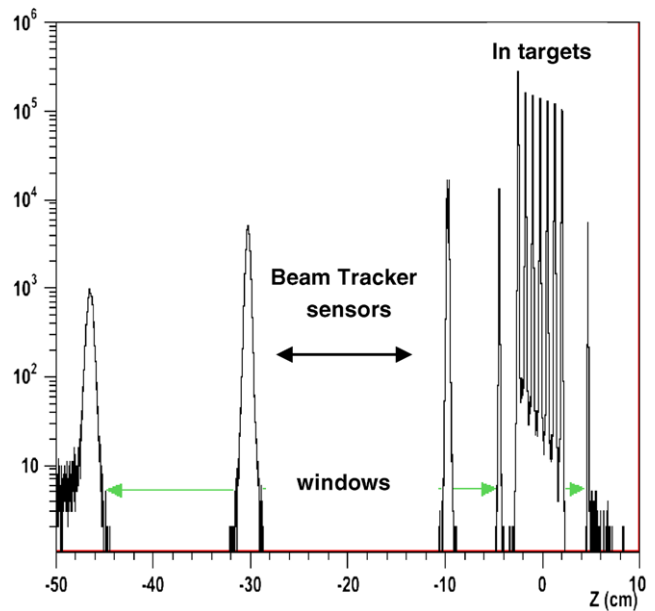

Fig. 3 Longitudinal coordinate of interaction point

3.1 Event reconstruction and selection

As a first step, the muon tracks are reconstructed in the muon spectrometer. About half of the triggers are discarded either because it was not possible to reconstruct two muons or because at least one of the muons traversed the 4-m-long iron poles of the ACM. These tracks suffer from a very strong multiple scattering, which would severely degrade the momentum resolution. The muon tracks reconstructed in the muon spectrometer are then extrapolated back to the target region and matched to the tracks reconstructed in the vertex spectrometer. This is done comparing both their angles and momenta, requiring a *matching* χ^2 less than 3. Once identified, the muons are refitted using the joint information of the muon and the vertex spectrometers. These tracks will be referred to as *matched muons*. Muon pairs of opposite charge are then selected. The matching technique drastically improves the signal-to-background ratio and the dimuon mass resolution, which decreases from ~80 MeV (using only the information from the muon spectrometer) to ~20 MeV at the ϕ peak, independent of centrality [40].

Events with more than one interaction vertex or with a (reconstructed) charged track multiplicity smaller than 4 are discarded [40]. The matched dimuon mass spectrum is shown in the left panel of Fig. 4. The same picture shows also the two background sources: combinatorial and fake matches. These are discussed in detail in the next subsection. As it can be seen, the dominant background is the combinatorial background—the fake match background is almost one order of magnitude smaller. The ω and ϕ peaks are very well resolved and the η peak is also visible. The right panel of Fig. 4 shows an expanded view of the ω and
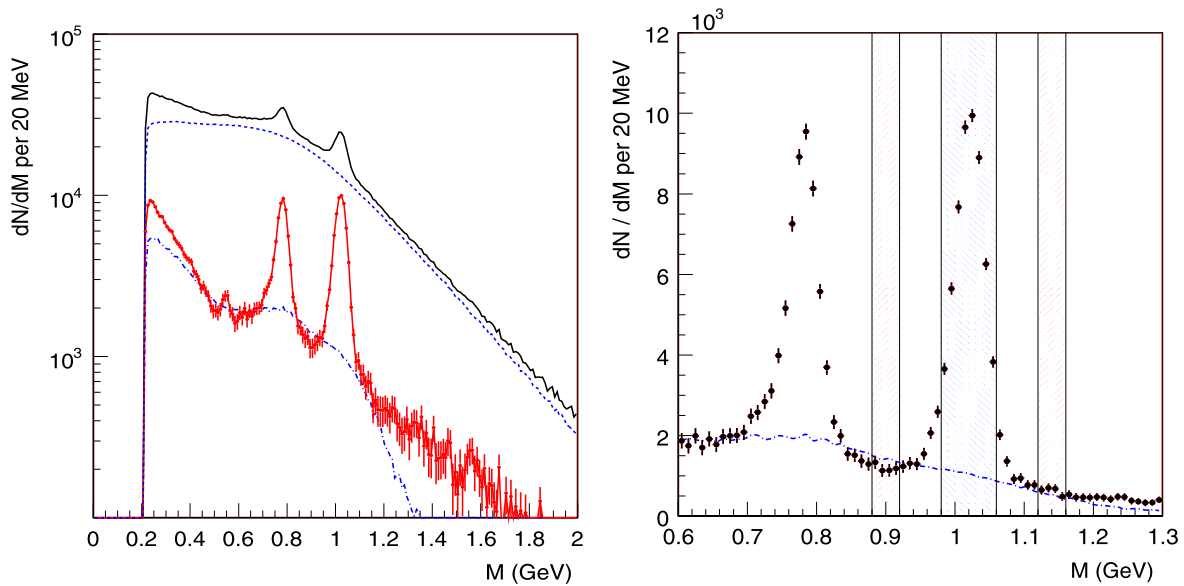
Fig. 4 *Left panel*: raw mass distribution (*continuous line*), combinatorial background (*dashed line*), fake tracks (*dot-dashed line*) and mass distribution after combinatorial background and fake tracks subtraction (*continuous curve with error bars*). *Right panel*: mass region around the ϕ peak and mass windows used in the analysis after backgrounds subtraction. The *dot-dashed* distribution is the total fake matches distribution

ϕ region after the subtraction of backgrounds. The sample consists of ∼70 000 ϕ events. The signal/background ratio, integrated over centrality, is ∼1/3 below the ϕ peak, ranging from about 3 in peripheral events to about 1/5 in central ones.

To study ϕ production, events in a small mass window centered at the ϕ pole mass ($0.98 < M < 1.06$ GeV) are selected from the mass distribution after the combinatorial background subtraction. The continuum below the ϕ is accounted subtracting the events in two side mass windows ($0.88 < M < 0.92$ GeV and $1.12 < M < 1.16$ GeV), shown in the right panel of Fig. 4.

No specific cuts in transverse momentum, rapidity or Collins–Soper angle are applied. As already mentioned, the detector introduces an intrinsic rapidity cut $3 \lesssim y \lesssim 4.2$ at the ϕ mass.

3.2 Background subtraction

The dimuon sample is affected by two sources of background: the combinatorial background and the *fake* matches. The former is the contribution of uncorrelated muon pairs, mostly coming from the decay of pions and kaons, and is subtracted with an event mixing technique [40, 41]. The NA60 apparatus triggers also on like-sign pairs ($\mu^- \mu^-$ and $\mu^+ \mu^+$), which, at SPS energies, contain only uncorrelated muons. Two muons from different like-sign events are randomly paired to build a dimuon sample which is uncorrelated by construction. The comparison of the real and mixed

spectra for the like-sign pairs leads to an estimate of the accuracy of the background subtraction of ∼1% over the full dimuon mass spectrum. The like-sign sample is also used to determine the absolute normalization of the combinatorial background [40, 41]. The combinatorial background is shown as a dashed line in the left panel of Fig. 4.

The background from fake track matches comes from the fact that, when the multiplicity is high, a muon track can be associated to more than one track in the vertex telescope with an acceptable matching χ^2, and the track with the lowest χ^2 may not be the correct match. It can also happen that the correct track in the vertex telescope in absent altogether. The contribution of the fake matches can be estimated in two different ways. The first approach is an overlay Monte Carlo technique, where a Monte Carlo dimuon is reconstructed on top of a real event. Selecting the match with the smallest matching χ^2 it is possible to determine the fraction of fake matches as a function of mass, transverse momentum, etc. The left panel of Fig. 5 shows the matching χ^2 for the correctly matched tracks and for the fake matches, as obtained with an overlay Monte Carlo simulation. The stricter the matching χ^2 cut, the higher the signal to background ratio will be. However, a tight cut reduces significantly the statistics. The second method is based on the event mixing technique, which extracts the probability distributions of fake matches from real data alone. The basic idea is to match the tracks in the muon spectrometer from one event to the vertex tracks of a different event [40, 41]. All the matches obtained in this way are fake by construction. The two methods agree within 5%.

6

Eur. Phys. J. C (2009) 64: 1–18
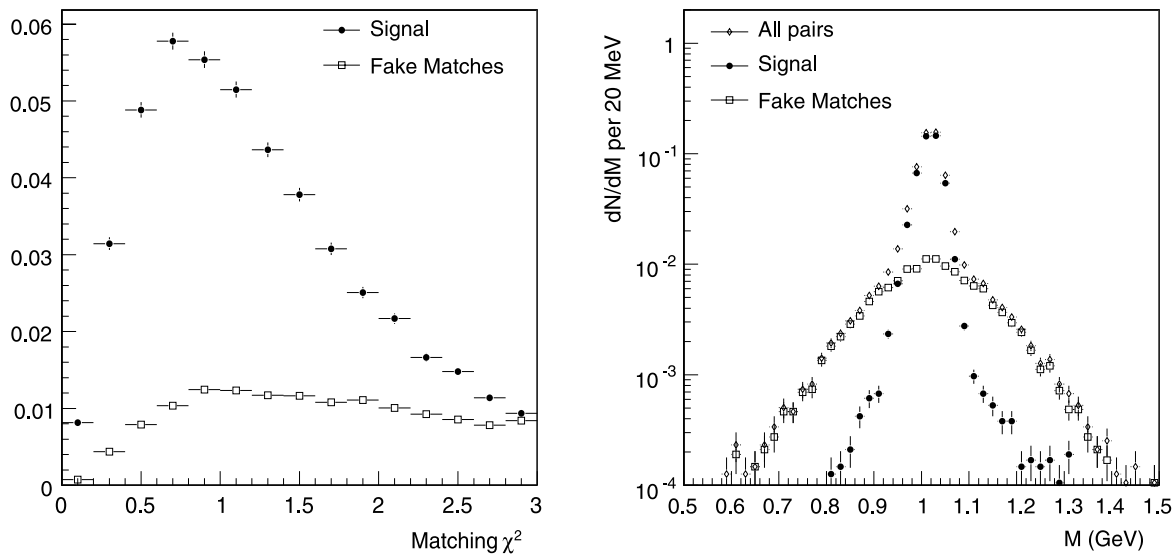
Fig. 5 Matching χ^2 (*left*) and mass distribution (*right*) of signal and fake matches for simulated ϕ events

The right panel of Fig. 5 shows the Monte Carlo dimuon invariant mass for ϕ events when one or both muons are not correctly matched, for signal events and for all reconstructed pairs. This gives an idea how incorrect matching degrades the kinematics, resulting in a broadened ϕ peak with $\sigma \sim 100$ MeV. Notice however, that this is not the total fake matches background under the ϕ peak, because also other processes can contribute—continuum from open charm or tails from the $\rho - \omega$ region. The total fake matches distribution is shown in detail as a dashed line in the right panel of Fig. 4. This shows that the fake matches, in the specific case of the ϕ meson, can also be directly eliminated by the subtraction of the side windows, without the need to estimate them with the methods outlined above.

In the following, the analysis is repeated subtracting the fakes both with the event mixing technique and with the side windows.

3.3 Centrality selection

All results are studied as a function of the collision centrality. Events are divided into five centrality bins by using the charged tracks multiplicity as summarized in Table 1. The reconstructed minimum bias multiplicity distribution depends on the target because of acceptance, reconstruction efficiency and secondary particles contamination. The distributions in the seven targets are rescaled so that they overlap to that in the first target. The latter is then fitted with the multiplicity distribution obtained with a Glauber Monte Carlo simulation, assuming that the number of reconstructed tracks is proportional to the number of participants, with a smearing due to the resolution and inefficiencies of the detector. It is assumed that the effects due to acceptance, reconstruction efficiency and secondaries are embedded in the

Table 1 Centrality bins used in the analysis, selected using the charged tracks multiplicity. The intervals used in the five centrality bins are reported in the table, together with the mean values of the number of participants (N_{part}) and of the number of binary collisions (N_{coll}) (see text for details)

$dN_{ch}/d\eta$ range	$\langle N_{part}\rangle$	$\langle N_{coll}\rangle$
4–25	15	14
25–50	41	49
50–95	78	110
95–160	133	218
160–250	177	317

proportionality constant and smearing factor. The distributions and mean values of the number of participants N_{part} and of the number of binary collisions N_{coll}, are obtained applying the same multiplicity cuts used in the real data to the simulated data. Alternatively, the real data can be corrected for acceptance, reconstruction efficiency and secondaries using a Monte Carlo simulation [42, 43]. The number of measured tracks can be thus converted to the number of primary particles event by event, as a function of target and centrality. The distribution of primaries is then matched to the distribution of N_{part} obtained by a Glauber Simulation. We find $N_{part} \simeq dN_{ch}/d\eta|_{3.7}$ [40, 44].

The difference on the mean N_{part} and N_{coll} values for each bin obtained with the two methods is taken as an estimate of the systematic uncertainty and is found to be about 10% for the peripheral bins and 5% for the central bins.
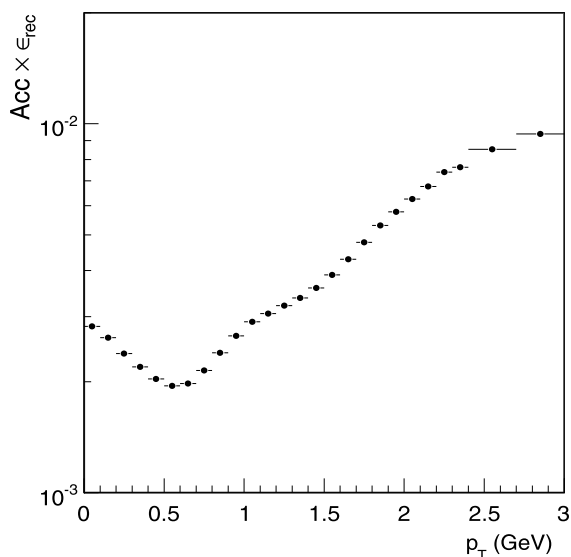
3.4 Acceptance and reconstruction efficiency correction

After subtraction of the combinatorial background, the physical continuum and the fake tracks, the data are cor-

rected for acceptance and reconstruction efficiency. These are estimated with an overlay Monte Carlo simulation, using the real hit occupancy in the detector superimposed to Monte Carlo muon pairs. The same cuts used for the real data were applied to the simulated data. An overall 95% efficiency was assumed for the pixel detector. The input sources' kinematics are generated using the Genesis event generator [45], tracked through the apparatus using GEANT 3.21 and reconstructed using the NA60 analysis framework.

The study of the differential spectra would require a multi-dimensional acceptance correction in rapidity, transverse momentum and Collins–Soper angle. Since the low populated bins in the phase-space corners can introduce large errors, a fiducial cut should be applied, at the cost of reducing the effective statistics. To avoid this loss, a one-dimensional correction is applied to each kinematic variable under study, integrating over the remaining ones. This requires a careful tuning of the Monte Carlo input kinematics, which was adjusted with an iterative procedure to the measured distributions for each of the five centrality bins. To validate this procedure, the full analysis chain (event selection, reconstruction, acceptance correction, fitting) is applied to Monte Carlo events. It is verified that the corrected kinematic distributions and the estimated parameters are consistent with those used as input in the Monte Carlo.

The acceptance times reconstruction efficiency for the ϕ as a function of p_T is shown in Fig. 6. The apparatus has a good acceptance down to zero p_T, due to the additional dipole field in the vertex region. Indeed, low mass and low p_T dimuons, which would not be accepted by the muon spectrometer, are bent into the acceptance by the vertex dipole magnet, as opposed to NA50, which used the same muon spectrometer, but had no acceptance for

Fig. 6 Geometrical acceptance times reconstruction efficiency as a function of p_T for the ϕ

$p_T \lesssim 1.1$ GeV. Further details on the rapidity and angular-distribution acceptance will be given in the specific subsections on the results.

3.5 Systematic effects

The main sources of systematic error are the uncertainties on the input parameters of the Monte Carlo simulation (which reflect on an uncertainty in the acceptance) and on the estimate of the physical background below the ϕ. The former is estimated by changing the values of the parameters in the input Monte Carlo within 1σ of the measured value. The latter, by varying the side windows offset (from 50 MeV to 70 MeV) and width (from 30 MeV to 50 MeV). The contributions from these two factors are added in quadrature. Uncertainties in the combinatorial background and in the fake matches subtraction play a small role here, as the ϕ peak is very well resolved.

Several consistency checks were performed to test for the presence of hidden systematic effects [46]: the matching χ^2 cut was varied between 2 and 3, the kinematic cuts $2.9 < y < 3.9$ and $|\cos\theta_{CS}| < 0.5$ were applied, the analysis was repeated independently in the 4 ACM/PT7 fields' combinations, a two-dimensional acceptance correction (vs. y and p_T) was used and the different methods for fake subtraction were implemented. Most of those checks did not lead to significantly different results, with the exception of the matching χ^2 cut variation. This leads to a small but not negligible difference, which is added in quadrature to the systematic error. This difference is most likely due to the uncertainty in the energy loss compensation or to a small residual misalignment in the pixel telescope planes. The results on the yield, mass and width are affected by further sources of systematics, due to the parameters needed for their computation. Details are given in Sect. 4.4 and in Sect. 4.6. The number of participants estimated with the Glauber model is affected by a 10% uncertainty in the peripheral bins, which decreases to ∼5% in the most central, as explained in Sect. 3.3.

## 4 Results

4.1 Rapidity

The rapidity acceptance for $0 < p_T < 0.5$, $0.5 < p_T < 1$ and $p_T > 1$ GeV is shown in Fig. 7. The apparatus has acceptance in the interval 3–4.2 depending on the target. There is a small correlation $y - p_T$ such that low y tends to select larger p_T. The rapidity is studied as a function of centrality and the width estimated with a Gaussian fit in the range $3.2 < y < 4.1$. The midrapidity value is fixed to 2.91. The width as a function of centrality is shown in Fig. 8 (left panel) and within the errors one can deduce either a constant or a slightly decreasing trend. The rapidity distribution
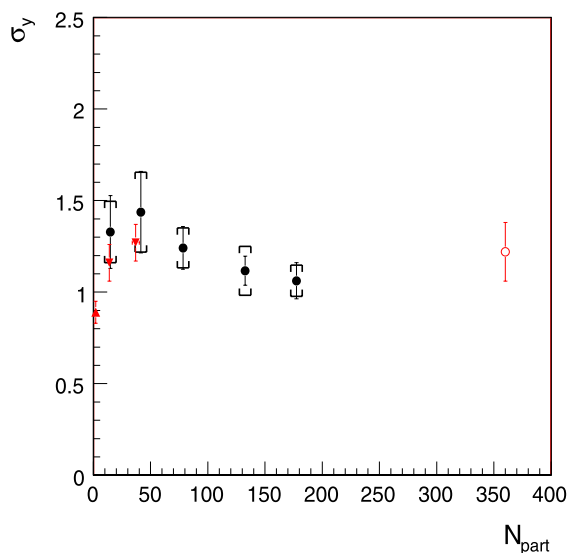
8

Eur. Phys. J. C (2009) 64: 1–18

integrated in centrality is shown in Fig. 8 (right panel). The resulting width is $1.13 \pm 0.06 \pm 0.09$. This is in agreement with previous NA49 measurements in other collision systems at the same energy [19, 20], as shown in Table 2.

4.2 Angular distributions

In general, the angular distribution of the decay muons in the ϕ meson rest frame can be related to the elements of the spin density matrix.
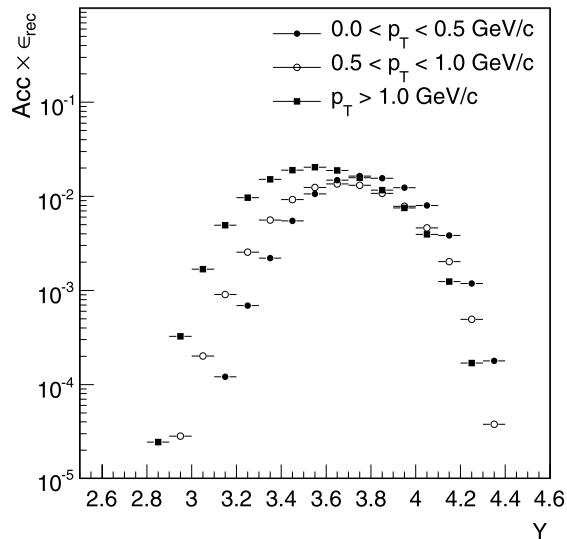
Fig. 7 Geometrical acceptance times reconstruction efficiency as a function of y for the ϕ for $0 < p_T < 0.5$, $0.5 < p_T < 1$ and $p_T > 1$ GeV
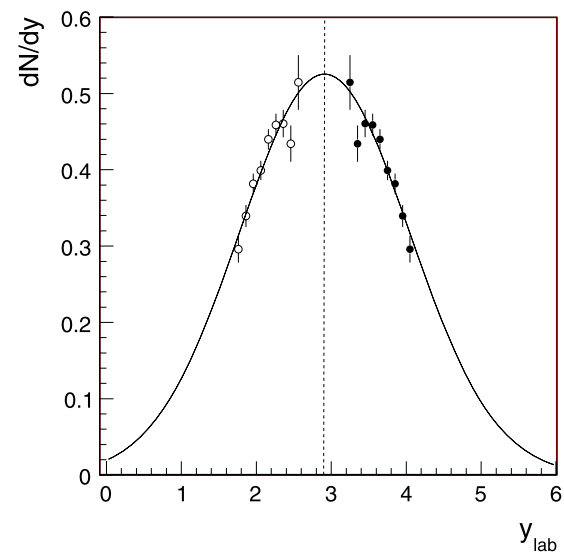
In this paper the inclusive $dN/d\cos\theta$ distributions are studied as a function of transverse momentum and centrality. The polar angle θ is the angle between the μ^+ and the z axis as measured in the following three widely used reference frames. In the helicity frame, the axis is defined as the direction of flight of the ϕ meson in the target–projectile rest frame. In the Gottfried–Jackson frame (GJ), the axis is defined as the projectile direction in the ϕ rest frame [47]. Finally, in the Collins–Soper frame (CS) the axis is given by the bisector of the projectile and the negative target direction in the ϕ rest frame [48].

In all the three frames, the ϕ acceptance as a function of $\cos\theta$ has a strong dependence on transverse momentum. In particular, the apparatus has zero acceptance for high $|\cos\theta|$ and low p_T. The acceptance vs. $\cos\theta$ for the p_T windows $0 < p_T < 0.5$, $0.5 < p_T < 1$ and $p_T > 1$ GeV, is shown in Fig. 9 for the CS and GJ frames. The most critical situation occurs for the Collins–Soper angle, while the helicity frame is similar to the GJ frame.

Table 2 Gaussian width of the rapidity distribution of the ϕ meson in several collision systems, at 158 AGeV incident beam energy. The second quoted error for the NA60 point is the systematic error

Experiment	System	σ_y
NA49	p–p	0.89 ± 0.06
NA49	C–C	1.16 ± 0.10
NA49	Si–Si	1.27 ± 0.10
NA60	In–In	$1.13 \pm 0.06 \pm 0.09$
NA49	Pb–Pb	1.22 ± 0.16

Fig. 8 *Left panel*: Gaussian σ of the rapidity distribution of the ϕ meson, as a function of centrality; *full circle*: $\phi \to \mu\mu$ in In–In (NA60); *full upward triangle*: $\phi \to K^+K^-$ in p–p (NA49); *full downward triangle*: $\phi \to K^+K^-$ in C–C and Si–Si (NA49); *open circle*:

$\phi \to K^+K^-$ in Pb–Pb (NA49). *Right panel*: rapidity distribution of the ϕ meson; *open symbols* are obtained reflecting the measured points around mid-rapidity

Eur. Phys. J. C (2009) 64: 1–18

9

The $dN/d\cos\theta$ distribution is fitted with the function $1 + \lambda \cdot \cos^2\theta$, where the parameter λ is related to the degree of polarization. The spectra, integrated in centrality and p_T, are shown in the left panel of Fig. 10. The polarizations obtained from the fits are zero within errors in all cases: $\lambda_{\text{HEL}} = -0.07 \pm 0.06 \pm 0.06$, $\lambda_{\text{GJ}} = -0.07 \pm 0.06 \pm 0.06$, $\lambda_{\text{CS}} = -0.13 \pm 0.07 \pm 0.06$.

The polarization is then studied differentially in the three p_T windows $0 < p_T < 0.5$, $0.5 < p_T < 1$ and $p_T > 1$ GeV, without centrality selection. No significant deviations from the p_T integrated values are found.

The results as a function of centrality and integrated in p_T are shown in the right panels of Fig. 10. The polarization is compatible with zero in the helicity and Gottfried–
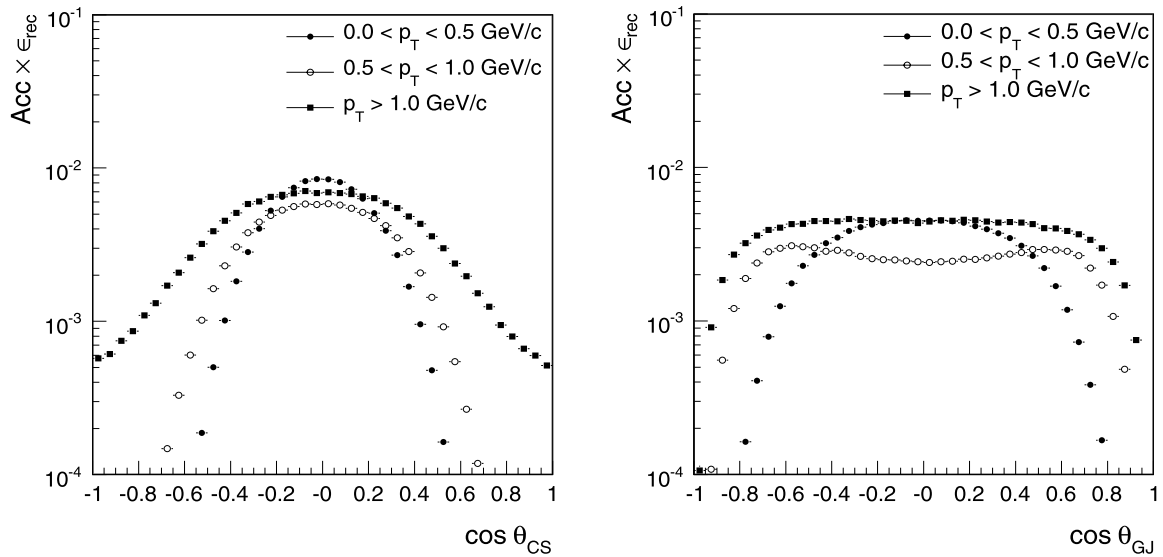
Fig. 9 Geometrical acceptance times reconstruction efficiency as a function of $\cos\theta$ for the ϕ for $0 < p_T < 0.5$, $0.5 < p_T < 1$ and $p_T > 1$ GeV in the CS frame (*left*) and in the GJ frame (*right*)
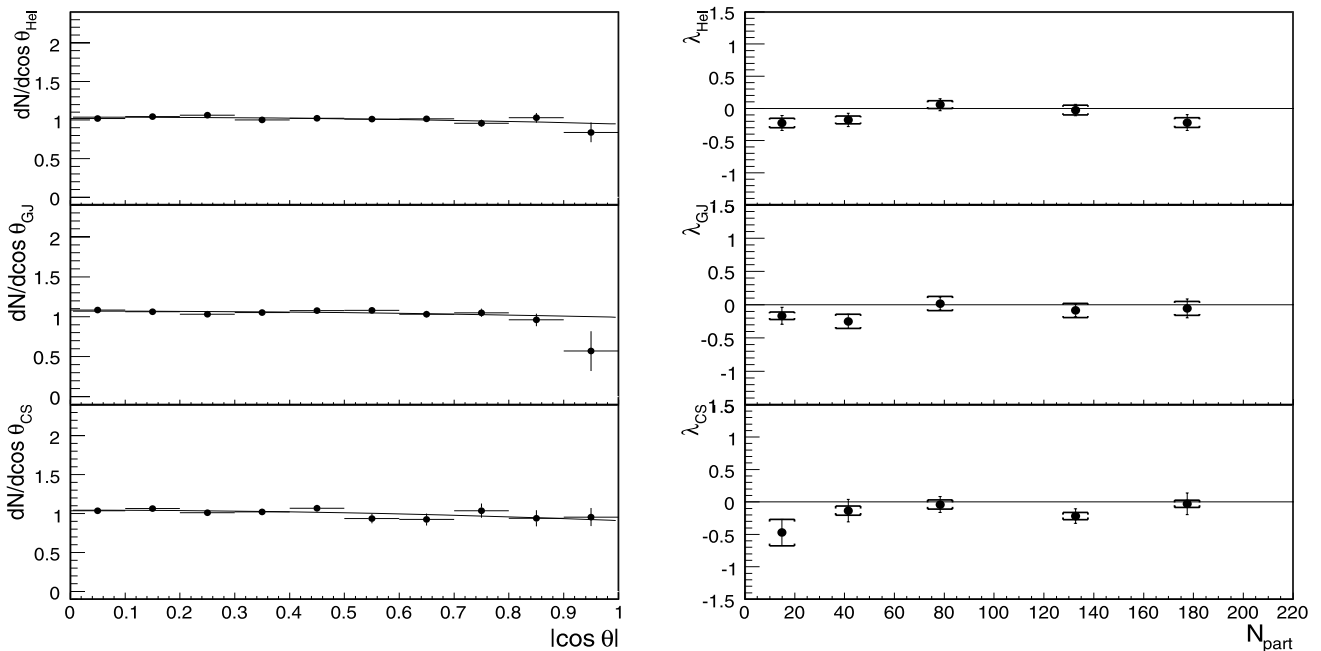
Fig. 10 Angular distributions of the ϕ, measured in the helicity, Gottfried–Jackson and Collins–Soper frames. *Left panels*: angular distributions integrated in centrality. *Right panels*: polarization as a function of centrality

Jackson frames, independent of centrality. In the Collins–Soper frame there is a hint for a negative polarization in the most peripheral bin. However, this is within 2σ compatible with zero and then consistent with the absence of any effect as seen in the other frames.

These results as a function of p_T and centrality are consistent with the results integrated in centrality with $p_T >$ 0.6 GeV reported in a previous analysis by NA60 [29]. They show the absence of polarization, supporting the fact that particles are produced from a thermalized medium. The absence of polarization extends down to peripheral events, suggesting that it could be zero also in elementary collisions at this energy.

4.3 Transverse momentum

The acceptance and efficiency corrected transverse mass distributions are shown in the left panel of Fig. 11 for the different collision centralities, normalized in absolute terms.

The transverse momenta are first fitted in the range $0 < p_T < 3$ GeV with the thermal ansatz:

$$\frac{1}{m_T}\frac{dN}{dm_T} = \frac{1}{p_T}\frac{dN}{dp_T} \propto \exp(-m_T/T_{\text{eff}}). \qquad (1)$$

The effective temperature T_{eff} as a function of the number of participants is depicted in the right panel Fig. 11. In general one can notice that the T_{eff} shows an initial rise followed by a saturation in the most central bins.

The exponential form assumes thermal emission from a static source. In heavy-ion collisions, this is not correct due to the presence of radial flow, but (1) was nevertheless used by several experiments to fit the data. Since the m_T distributions are not purely exponential. The T_{eff} extracted from an exponential fit will depend in general on the fitted p_T range. It can be shown that, at first order, the T_{eff} value at low p_T is given by $T_{\text{eff}} \sim T_0 + m\beta_T^2$, where T_0 is the temperature at freeze-out, m is the particle mass and β_T is the average transverse velocity of the expanding source [49]. At high p_T, on the other hand, the T_{eff} extracted from the exponential fit is approximated by $T \sim T_0\sqrt{(1+\beta_T)/(1-\beta_T)}$ [49]. Thus, what is measured is a p_T dependent effective temperature, larger than the freeze-out temperature because of the radial flow.

The influence of radial flow is investigated by repeating the fits in two sub-ranges $0 < p_T < 1.6$ GeV (low p_T) and $1.1 < p_T < 3$ GeV (high p_T), which also correspond to the experimental windows covered by the NA49 and NA50 experiments, respectively. Since the statistics in the peripheral data at high p_T is limited, the two most peripheral bins are integrated for the fit in the high p_T range. The numerical values of T_{eff} as a function of centrality and of the different fit ranges are summarized in Table 3. An increase of the average T_{eff} can be noticed when the fit is restricted to the low p_T range, while a flatter trend is observed from the fit in the high p_T range. The difference between the effective temperatures obtained in the two fit ranges is around 10 MeV (average over the three most central bins). This pattern indicates the presence of radial flow but it is rather small, as expected from the small coupling of the ϕ to the "pion wind" [50, 51].

Further quantitative insight has been gained studying the spectra in the framework of the blast-wave model [52]:

$$\frac{dN}{m_T dm_T} \propto \int_0^R r\,dr\,m_T I_0\left(\frac{p_T \sinh\rho}{T_0}\right) K_1\left(\frac{m_T \cosh\rho}{T_0}\right),$$
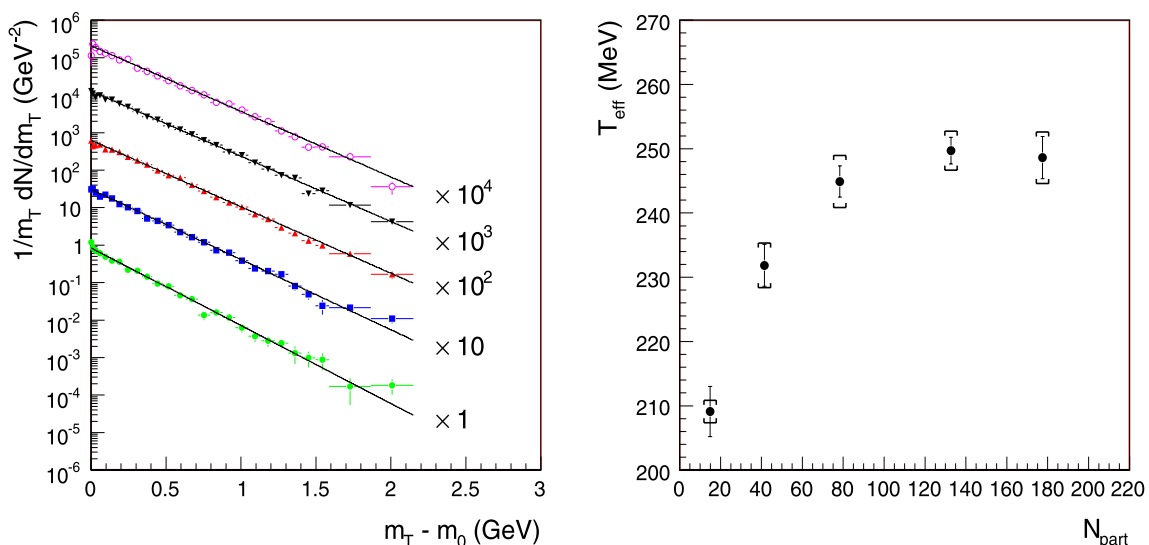
Fig. 11 *Left panel*: ϕ transverse mass distributions in indium–indium collisions as a function of centrality; *from top to bottom*: central to peripheral spectra. *Right Panel*: Centrality dependence of the T_{eff} parameter; fit performed over the full NA60 range ($0 < p_T < 3$ GeV)

Table 3 Centrality dependence of the T_{eff} parameter in different fit ranges. The second quoted error is the systematic error

$\langle N_{\text{part}} \rangle$	T_{eff} (MeV) $0 < p_T < 3$ GeV	T_{eff} (MeV) $0 < p_T < 1.6$ GeV	$\langle N_{\text{part}} \rangle$	T_{eff} (MeV) $1.1 < p_T < 3$ GeV
15	$209 \pm 4 \pm 2$	$206 \pm 5 \pm 2$	24	$228 \pm 6 \pm 4$
41	$232 \pm 3 \pm 3$	$229 \pm 5 \pm 2$		
78	$245 \pm 2 \pm 4$	$253 \pm 5 \pm 9$	78	$237 \pm 5 \pm 1$
133	$250 \pm 2 \pm 3$	$258 \pm 5 \pm 5$	133	$245 \pm 4 \pm 5$
177	$249 \pm 3 \pm 4$	$253 \pm 8 \pm 11$	177	$244 \pm 5 \pm 3$

$$\tag{2}$$

where $\rho = \tanh^{-1} \beta_r(r)$ and a linear velocity profile was assumed: $\beta_r = \beta_s(r/R)$. The slopes of the p_T spectra define lines in the $T_0 - \beta_T$ plane. T_0 is varied in the window 90–140 MeV. Transverse momentum distributions are then generated using (2), with β_T values tuned in order to reproduce the observed T_{eff} values. Figure 12 shows the results for the ϕ and also for the negative charged hadrons (essentially pions), η, ω and ρ [51]. The study is performed for $p_T > 0.4$ GeV in order to exclude the rise in the low p_T region seen in the ρ excess spectra [53]. In addition, to perform a comparison with meaningful statistical accuracy with the other particles, data were integrated in centrality, excluding the most peripheral events. A clear hierarchy in the freeze-out parameters, as a consequence of the particle coupling to the medium is visible. The ϕ is the least coupled particle, while the ρ, being continuously produced in the medium via $\pi^+\pi^-$ annihilation is maximally coupled. The freeze-out component of the ρ receives the strongest radial flow boost, with a $T_{\text{eff}} > 300$ MeV, 50 MeV above the ϕ [51, 53].
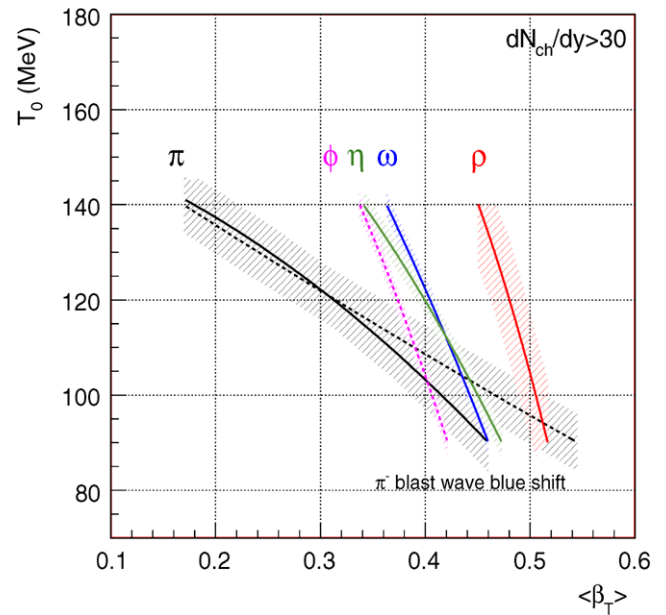
4.4 Yield

The average number of ϕ mesons per interaction $\langle \phi \rangle$ is evaluated using the J/ψ as a reference process. Once corrected for anomalous and nuclear absorption, $\langle J/\psi \rangle$ scales with the number of binary collisions and can be written as

$$\langle J/\psi \rangle_{\mu\mu} = \left(\sigma_{\text{NN}}^{J/\psi,\mu\mu} / \sigma_{\text{NN}} \right) \cdot N_{\text{coll}}. \tag{3}$$

Here $\sigma_{\text{NN}}^{J/\psi,\mu\mu} = 5.64 \pm 0.1$ nb is the J/ψ cross section in nucleon–nucleon collisions multiplied for the $J/\psi \to \mu\mu$ branching ratio. It was derived by the systematic study of J/ψ production in pA collisions performed at 400 and 450 GeV, rescaling to 158 GeV and extrapolating to full phase space [54]. The estimated nucleon–nucleon inelastic cross section at $\sqrt{s} = 17.2$ GeV is $\sigma_{\text{NN}} = 31.7 \pm 0.5$ mb [55].

$\langle \phi \rangle$ can be evaluated from the experimental ratio

$$\frac{\langle \phi \rangle}{\langle J/\psi \rangle_{\mu\mu}} = \frac{N_\phi / (A_\phi \times \varepsilon_{\text{rec}}^\phi \times \text{BR}_{\mu\mu}^\phi)}{N_{J/\psi} / (A_{J/\psi} \times \varepsilon_{\text{rec}}^{J/\psi} \times f_{J/\psi}^{\text{Abs}})} \tag{4}$$

Fig. 12 Blast-wave analysis results for η, ρ, ω, ϕ and negative hadrons (pions). Fits performed in the range $0.4 < p_T < 1.8$ GeV

where $N_{\phi(J/\psi)}$ is the number of ϕ (J/ψ) mesons observed in a given centrality bin, $A_{\phi(J/\psi)} \times \varepsilon_{\text{rec}}^{\phi(J/\psi)}$ are the acceptance and reconstruction efficiency, $\text{BR}_{\mu\mu}^\phi$ is the $\phi \to \mu\mu$ branching ratio and $f_{J/\psi}^{\text{Abs}}$ incorporates the J/ψ nuclear and anomalous absorption factors. The same centrality bins, selected using charged particle multiplicity as described in Sect. 3.3, were used for both the ϕ and the J/ψ. Invoking lepton universality, the value 2.97×10^{-4} measured in the $\phi \to ee$ channel is used for the branching ratio, since it is known with better precision [55]. The nuclear absorption was accurately determined by several measurements in pA collisions at 400 and 450 GeV [54]. The anomalous absorption was determined from the J/ψ analysis of the same In–In data sample [56]. The overall correction factor comes from the product of the nuclear and anomalous absorption. One has to notice that recent preliminary p–A results from NA60 showed the nuclear absorption at 158 GeV is larger than previously assumed [57]. However, since the anomalous absorption is defined relative to the nuclear one, the overall correction $f_{J/\psi}^{\text{Abs}}$ remains largely insensitive to rel-

12

Eur. Phys. J. C (2009) 64: 1–18

ative changes of these two factors. The systematic uncertainty arising from the anomalous and nuclear absorption is 11% [56]. This is the dominating source of systematic uncertainty in the analysis of the yield.

By multiplying the ratio in (4) by (3), one obtains $\langle \phi \rangle$ as a function of the number of binary collisions N_{coll}. The values of N_{coll} and of N_{part} for each centrality bin are obtained by fitting the multiplicity distribution with a Glauber model, as described in Sect. 3.3 and summarized in Table 1.

Processes having different scaling properties as a function of centrality, such as the ϕ and the J/ψ, in general give rise to different multiplicity distributions and this could introduce a bias when using wide centrality bins. The analysis was repeated with a much finer centrality binning and this potential bias was found to be negligible.

The multiplicity integrated in centrality is $\langle \phi \rangle = 1.411 \pm 0.026 \pm 0.14$.

The robustness of the measurement is checked repeating the analysis integrated in centrality, with a different method having largely independent systematics. The ϕ cross section is determined with the formula

$$\sigma_\phi = \frac{N_\phi}{L A_\phi \epsilon_{\text{rec}}^\phi \epsilon_{\text{ev}} \epsilon_{\text{trig}} \epsilon_{\text{DAQ}} \text{BR}_{\mu\mu}^\phi}, \tag{5}$$

where L is the integrated luminosity, ϵ_{ev} is the event selection efficiency, ϵ_{trig} is the trigger efficiency, ϵ_{DAQ} is the efficiency related to the DAQ live-time. The integrated luminosity is given by $L = N_{\text{inc}} N_{\text{tgt}}$, where N_{inc} is the number of incident ions as measured by the ZDC and Beam Tracker detectors, while N_{tgt} is the effective number of indium atoms in the target system [58]. The latter is affected by a systematic uncertainty of 10%, because the transverse profile of the beam is wider than the targets (except for the first one, which had a radius of 0.6 cm). The trigger efficiency was determined with special runs taken without the dimuon trigger. It is 81% and is affected by a 6% systematic error.

The average yield is then obtained dividing the cross section by the fraction of total In–In inelastic cross section, corresponding to the cut $N_{\text{ch}} > 4$, as estimated with the Glauber Monte Carlo (see Sect. 3.3). The total inelastic cross section calculated with the Glauber model is $\sigma_{\text{inel}}^{\text{InIn}} = 4.8$ b, and has a 10% uncertainty, mostly due to the uncertainties on the nuclear density profiles. The centrality integrated ϕ cross section is $\sigma_\phi = 6.83 \pm 0.08$ b. This leads to $\langle \phi \rangle = 1.73 \pm 0.02 \pm 0.27$, in agreement with the result based on the standard method, taking into account only the unrelated systematic errors in the two approaches.

The results as a function of centrality, obtained by taking the average of the two methods weighted by the systematic error, are summarized in Table 4. The ratio $\langle \phi \rangle / N_{\text{part}}$ is seen to increase with the collision centrality indicating the presence of an enhancement as in other collision systems.

Table 4 ϕ yield as a function of centrality. The bin by bin systematic error is reported in the table. The measurements are also affected by a 13% systematic uncertainty independent of centrality

| N_{part}	$\langle \phi \rangle$
14	$0.172 \pm 0.007 \pm 0.021$
41	$0.690 \pm 0.025 \pm 0.074$
78	$1.48 \pm 0.04 \pm 0.15$
132	$3.10 \pm 0.08 \pm 0.2$
177	$5.0 \pm 0.17 \pm 0.2$

4.5 Discussion of the results on T_{eff} and yield

As mentioned in the introduction, the discrepancies in absolute yields and T_{eff} values observed by NA49 and NA50 became historically known as the ϕ *puzzle* [14, 22]. To explain those differences, it was originally proposed that in-medium effects and kaon absorption or rescattering could prevent the reconstruction of in-matter $\phi \to K\bar{K}$ decays, in particular at low transverse momentum, while the ϕ mesons decaying in the lepton channel would not be affected. This would lead to reduced yields and enhanced T_{eff} values in the $K\bar{K}$ channel as compared to the $\mu\mu$ channel. In this section, all the measurements performed at the SPS, including the new one in In–In, are compared and the hypothesis of the physical mechanism described above is critically reviewed, considering the facts in favor of and against it.

Figure 13 shows the NA60 T_{eff} obtained performing the fits in the p_T windows corresponding to the coverage of NA49 (left) and NA50 (right). As mentioned in Sect. 4.3, the difference of the temperature in the two p_T windows in In–In is around 10 MeV, indicating a modest radial flow effect. Although a similar pattern is observed in Pb–Pb collisions—a stronger increase at low p_T (NA49) and a flattening at high p_T (NA50)—the maximum difference is, for the most central Pb–Pb collisions, about 70 MeV. This difference seems not to be consistent with the T_{eff} variation implied by radial flow as observed in the NA60 data.

In the common fit range, the NA60 T_{eff} values in In–In are ∼10 MeV larger than those measured by NA50, while there is a seeming agreement between NA60 and NA49 in the common fit range. However, the NA49 errors are large in this region and, in addition, a direct comparison of the values of T_{eff} between NA60 and the Pb–Pb experiments for the same N_{part} is not straightforward, due to the different geometry of the collision (the relative weight of the thin nuclear halo is higher in peripheral Pb–Pb collision than in a smaller system).

The temperature variation in different collision systems, when restricting to central collisions only, is shown in Fig. 14. This picture includes also the NA49 results for C–C, Si–Si and the CERES result in the kaon channel for central Pb–Pb (the dielectron measurement has a very large error).
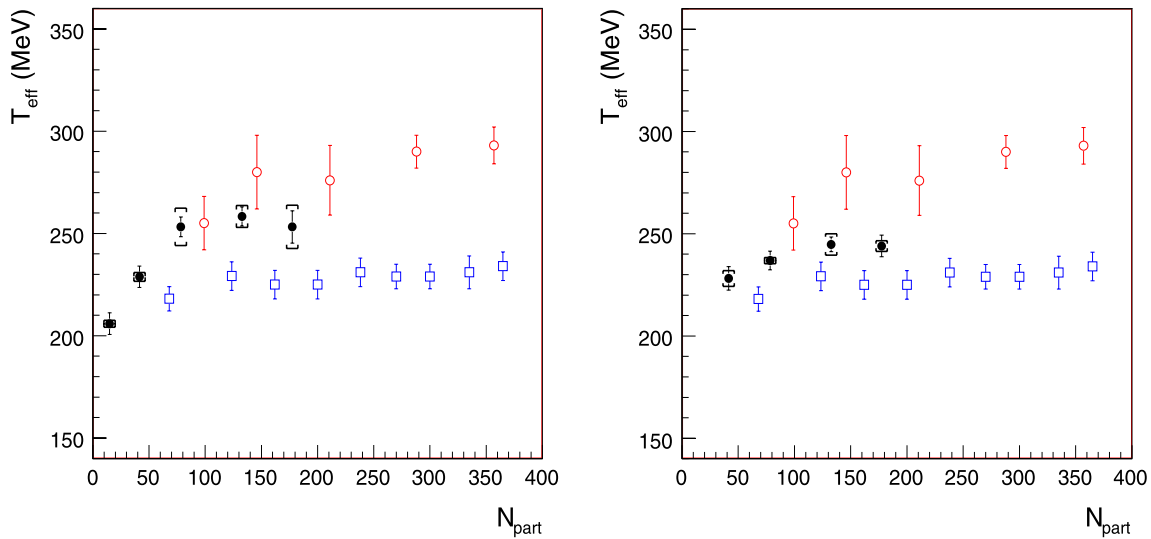
Fig. 13 Centrality dependence of the T_{eff} parameter (*full circles*) compared to NA49 (*open circles*) and to NA50 (*open squares*). *Left panel*: fit performed in the NA49 range ($0 < p_T < 1.6$ GeV). *Right panel*: fit performed in the NA50 range ($p_T > 1.1$ GeV)
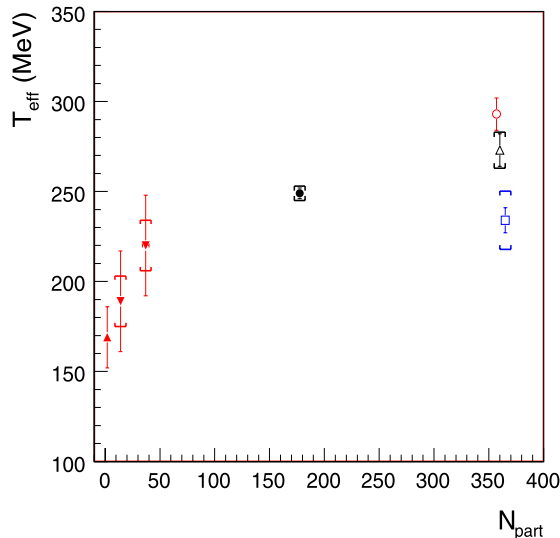
Fig. 14 T_{eff} for central collisions in several collision systems at 158 AGeV. *Full circle*: $\phi \to \mu\mu$ in In–In (NA60); *full upward triangle*: $\phi \to K^+K^-$ in p–p (NA49); *full downward triangle*: $\phi \to K^+K^-$ in C–C and Si–Si (NA49); *open circle*: $\phi \to K^+K^-$ in Pb–Pb (NA49); *open square*: $\phi \to \mu\mu$ in Pb–Pb (NA50); *open triangle*: $\phi \to K^+K^-$ in Pb–Pb (CERES)

The NA49 and CERES Pb–Pb points are above the In–In point by $\gtrsim 30$ MeV. Part of this difference can be related to radial flow, since in Pb–Pb a larger lifetime of the fireball would lead to a larger effect in central collisions. However, the T_{eff} measured for central Pb–Pb collisions is ~290 MeV, very close to that of the proton [59]. The blast-wave analysis of the NA60 data, on the other hand, shows a clear hierarchy in the freeze-out, with the ρ having a maximal flow due to its coupling to pions and the ϕ being the least coupled meson

(Fig. 12). The temperature of the freeze-out component of the ρ in In–In reaches 300 MeV or more, 50 MeV above the ϕ. One would therefore expect an even larger difference in Pb–Pb collisions between the T_{eff} of the ϕ and of the proton, which is strongly coupled to the pions via the Δ resonance and with a mass larger than the ρ. This suggests that the high T_{eff} seen by NA49 and CERES in the kaon channel cannot be ascribed entirely to radial flow.

The ϕ enhancement in In–In is compared to previous SPS measurements [18, 19, 21, 25] in Fig. 15.

An unambiguous comparison to the NA50 result in full phase space is not possible, due to lack of consensus on the value of the T_{eff} parameter in Pb–Pb collisions, but in general the NA50 enhancement is considerably higher than what is seen in In–In at any centrality. An extrapolation to full p_T with the NA50 T_{eff} values ($T \sim 220$–230 MeV independent of centrality) leads to values higher by a factor 2 or more with respect to In–In. Even extrapolating with the NA49 T_{eff} values ($T \sim 250$–300 MeV) would lead to values significantly higher (as shown by the continuous line in Fig. 15, the dashed lines represent the propagated uncertainty on these values).

The NA49 measurements[1] show that the $\langle\phi\rangle$ breaks N_{part} scaling and that $\langle\phi\rangle/N_{part}$, for central collisions as a function of the colliding system, already saturates for Si–Si. The ϕ enhancement in In–In is closer to NA49 than NA50, but it is not in agreement either. The two In–In most peripheral

---

[1]NA49 has characterized centrality of the collision using 2 quantities: the "number of wounded nucleons" and the "number of participants". The one directly comparable to our N_{part} is the number of wounded nucleons. The values for the different Pb–Pb bins are taken from Ref. [59].
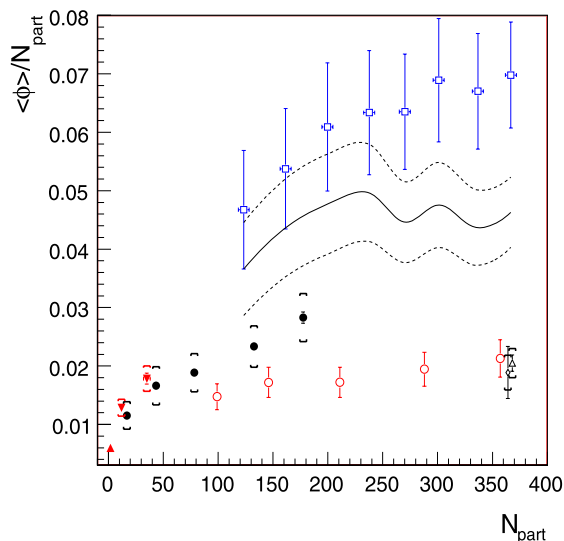
Fig. 15 $\langle\phi\rangle/N_{part}$ in full phase space in several collision systems at 158 AGeV. *Full circles*: $\phi \to \mu\mu$ in In–In (NA60); *full upward triangle*: $\phi \to K^+K^-$ in p–p (NA49); *full downward triangles*: $\phi \to K^+K^-$ in C–C and Si–Si (NA49); *open circles*: $\phi \to K^+K^-$ in Pb–Pb (NA49); *open squares*: $\phi \to \mu\mu$ in Pb–Pb (NA50); *open triangle*: $\phi \to K^+K^-$ in Pb–Pb (CERES); *open diamond*: $\phi \to ee$ in Pb–Pb (CERES). *Continuous line*: NA50 points extrapolated to full phase space with T_{eff} as measured by NA49, *dashed lines*: uncertainty on these points. *Square brackets*: systematic error (the error bar of the Pb–Pb data includes statistical and systematic error). C, Si and peripheral In points slightly displaced to improve readability

points are in agreement with C–C and Si–Si. However, for increasing centrality there is no saturation in In–In, while the NA49 Pb–Pb points show a flatter trend, which remains consistently smaller at any centrality. One could ask whether the increase of the yield ratio NA60/NA49 as a function of centrality could be ascribed to a suppression mechanism present in Pb–Pb that tends to decrease the overall enhancement. Restricting the comparison among In–In and Pb–Pb central collisions, the dimuon NA60 measurement remains larger than the kaon Pb–Pb points.

Summarizing, the large NA49/NA50 difference in central collisions for T_{eff} (70 MeV) and the yield (a factor 4), was hardly accounted for by theoretical models. A difference, though smaller, is also present in central collisions in T_{eff} and yield, when considering the NA60 muon measurement. This difference remains difficult to explain and hints for the presence of a physical effect. Whether this is present also in In–In, or peculiar only to Pb–Pb, would require the comparison to $\phi \to K\bar{K}$ in In–In. Preliminary NA60 results of $\phi \to K^+K^-$ suggest that there are no differences within the errors among the two channels in In–In [60].

One has to notice that the CERES dielectron and kaon points for central Pb–Pb are in agreement and in addition, both the NA50 T_{eff} and yield do not agree with NA60 either. Thus, at the moment it is not possible to include into a co-

herent picture all the measurements performed so far in the different collision systems.

4.6 Mass and width

As mentioned in the introduction, the spectral function of the ϕ could be modified in the medium, resulting in changes of its mass and width. The lifetime of the ϕ is 44 fm, larger than the estimated fireball lifetime ($\sim$7 fm). Any medium modified component would therefore sit under a large unmodified peak produced after freeze-out. In order to distinguish a possible in-medium component from instrumental effects, a careful tuning of the Monte Carlo simulation is required. This was not strictly necessary in previous analysis of the low mass region excess [51, 61], as this structure, mostly due to $\pi\pi \to \rho^* \to \mu\mu$, represents a large fraction of the total yield (the lifetime of the ρ is $\sim$1.3 fm).

Uncertainties in the detectors alignment, materials, energy loss compensation and precision of the magnetic field maps lead to residual differences between the Monte Carlo and the real data. These were compensated by fine-tuning the Monte Carlo against the peripheral data, where no in-medium effects are expected. The tuning was performed considering the whole mass spectrum below 1 GeV and required a global 0.3% ± 0.1% mass shift and a 4% ± 1% change in the mass resolution (previous NA60 analyses only included the mass shift correction). The uncertainties in this tuning are the main source of systematic error for the results discussed in this section.

In order to look for an in-medium component around the ϕ peak, the excess was isolated using the same subtraction procedure already extensively used for the low mass region [61]. The ω, ϕ and η Dalitz were subtracted from the total data using the Monte Carlo shapes and fixing the yield using solely local criteria; the ω Dalitz and the η two body were then subtracted by binding them to these processes via branching ratios. The quality of the subtraction can be judged in Fig. 16, which shows, for data integrated over centrality, the excess before and after the fine-tuning. While the tuning is essentially constrained by the narrow ϕ peak, it improves the subtraction over the whole mass spectrum: the evident artifacts visible in the left panel around all the narrow resonances (η, ω and ϕ) disappear after the tuning. The continuum left after the subtraction under the ϕ peak is smooth: no evidence for a medium modified ϕ can be seen in this figure. Indeed, an in-medium broadened component would manifest itself as broader tails extending to the sides. In this case, the subtraction of the vacuum component should not leave a smooth continuum, but rather a broad structure or a dip, which is not observed.

As mentioned in the introduction, the KEK-PS E325 experiment reported evidence for a large excess to the left of ϕ peak in p-Cu at 12 GeV for $\beta\gamma < 1.25$, corresponding

Eur. Phys. J. C (2009) 64: 1–18

15

to a produced ϕ moving very slowly inside the heavy target nucleus at rest. This situation is not directly comparable to the high energy regime discussed in this paper. Here, a fireball is produced with particle momenta boosted in the forward direction, therefore the relevant variable to select ϕ mesons mostly sensing the medium is transverse momentum. Moreover, in a high energy heavy-ion collision, as opposed to p–A, the ϕ can be produced not only at chemical freeze-out, but also in the hot hadronic medium via kaon reactions. Figure 17 shows the region around the ϕ mass peak for different p_T and centrality selections: the left panel shows the two most central bins and for $p_T < 0.6$ GeV, while the right panel shows the data integrated in centrality for $p_T < 0.2$ GeV. The continuum from the subtraction
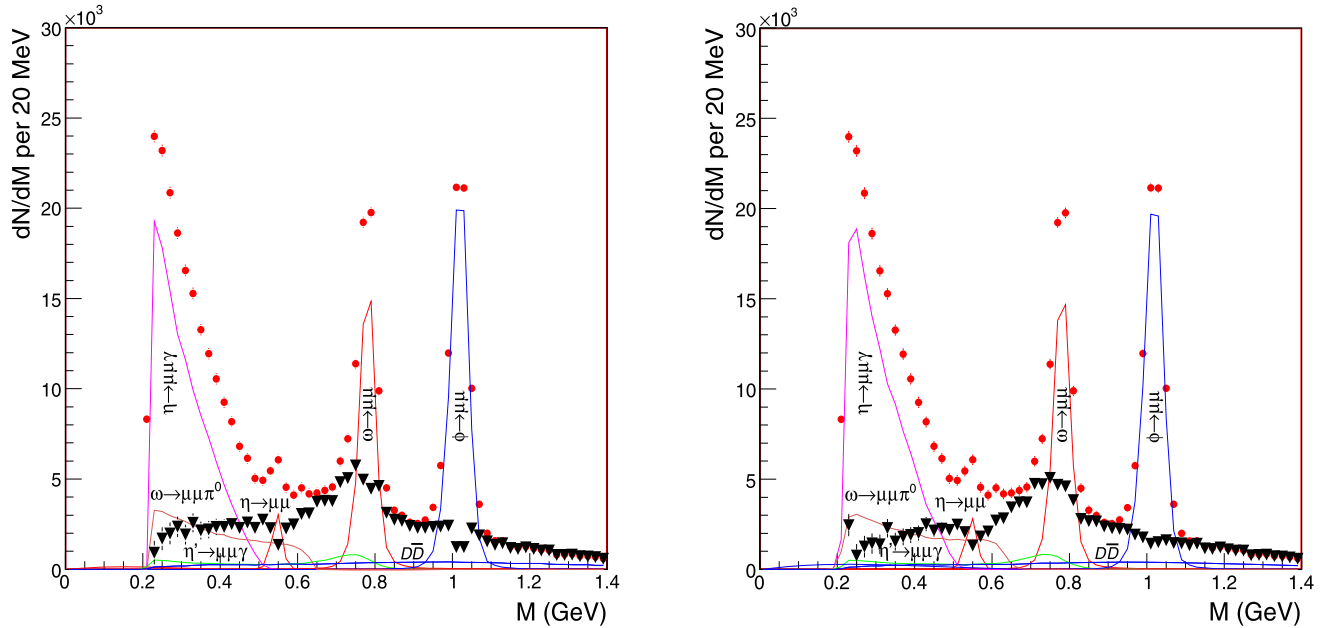
Fig. 16 Excess mass spectrum for data integrated in centrality, obtained without (*left*) and with (*right*) the Monte Carlo fine-tuning. *Red circles*: data; *black triangles*: excess data; *lines*: individual processes
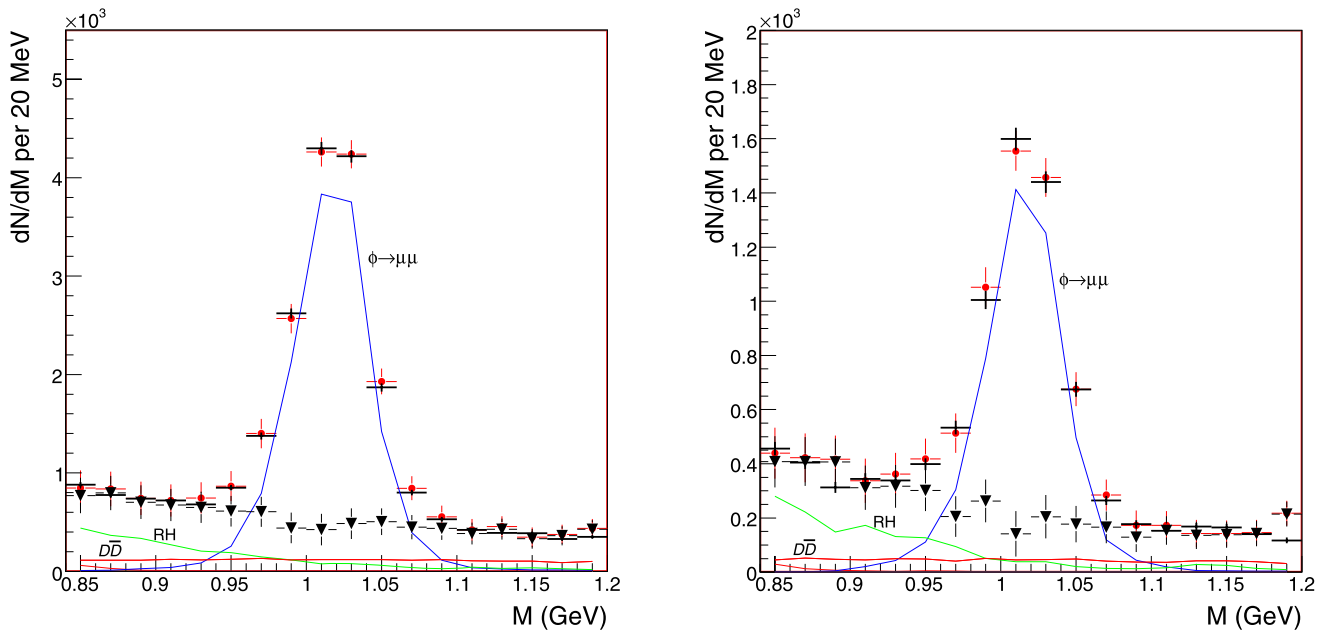
Fig. 17 ϕ mass region in the two most central bins for $p_T < 0.6$ GeV (*left*) and all centralities, $p_T < 0.2$ GeV (*right*). *Red circles*: data; *black triangles*: excess data; *lines*: individual processes (*RH*: model of Ref. [11]); *black crosses*: result of fit performed using the Monte Carlo shapes
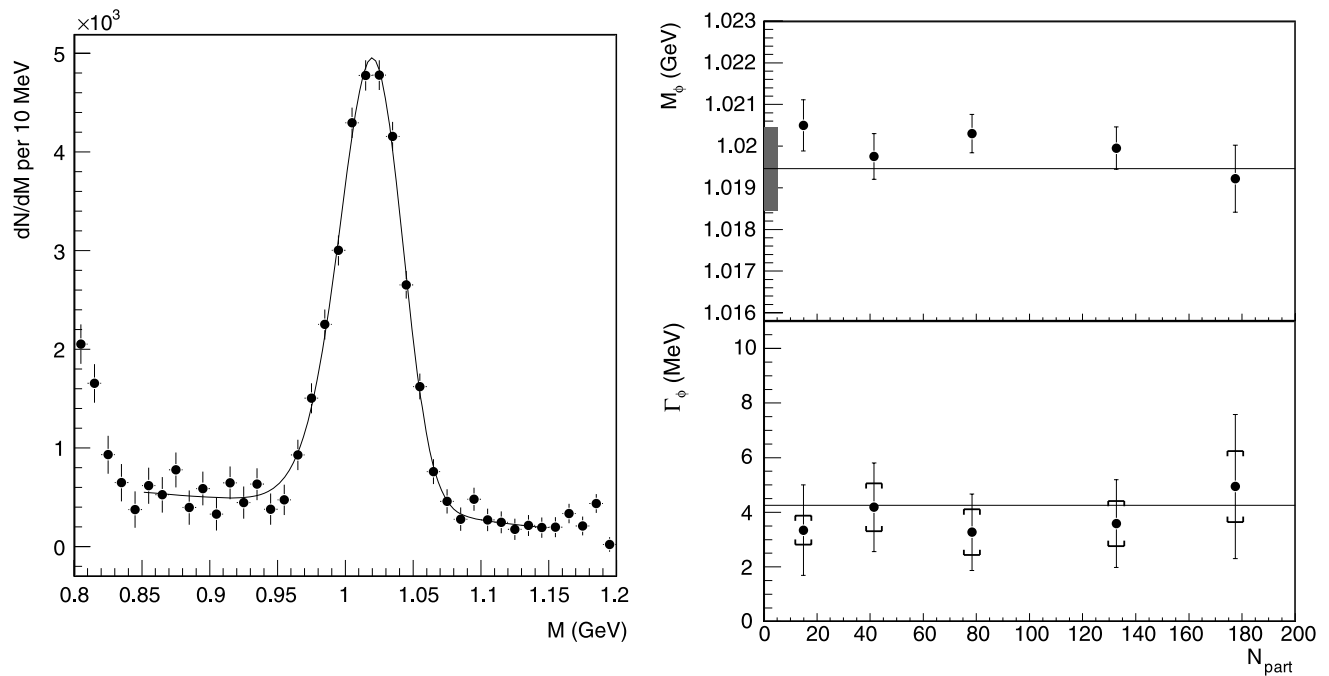
Fig. 18 *Left panel*: fit of the ϕ mass peak, semi-central bin ($N_{\mathrm{part}} = 133$) with a relativistic Breit–Wigner convoluted with the detector response, on top of a linear background. *Right panel*: mass (*top*) and width (*bottom*) of the ϕ as a function of centrality. *Shaded box*: systematic uncertainty common to all centrality bins

is smooth also in this case. Furthermore, a fit was performed using the Monte Carlo shapes for the different processes. The continuum was described with the model of Ref. [11], which includes, besides the in-medium ρ, multi-pion and partonic processes relevant in this mass region. The model of Ref. [62], having different weights for the multi-pion and partonic processes, does not change the conclusions, since it produces a similar yield below the ϕ peak. The χ^2/ndf is ~ 1 in all cases. There is no evidence of any mass shift or broadening, even at high centrality and low p_T, where one would expect to observe the strongest in-medium effects.

In order to estimate quantitatively the pole mass and total width of the ϕ peak, data were fitted with the convolution of a relativistic Breit–Wigner and of a function parameterizing the detector response, on top of a linear background. In a first step, the parameters of the detector response were adjusted on the Monte Carlo simulation. The data are then fitted leaving the mass and width of the Breit–Wigner as free parameters. The quality of the fit is very good, as shown in the left panel of Fig. 18, corresponding to the semi-central bin, $N_{\mathrm{part}} = 133$. The results on the mass and width as a function of centrality are shown in the right panel of Fig. 18. The systematic error was estimated changing the fit range, the background function and propagating the uncertainties in the Monte Carlo tuning. The mass and width are compatible with the PDG values and independent of centrality, although our sensitivity on the width is limited by the mass resolution, which is much larger than the natural width (this

is reflected in the large statistical error in the right panel of Fig. 18).

While the data can be described by a vacuum ϕ, we set an upper limit on a modified component using the only existing prediction for in-medium production of ϕ in 158 AGeV In–In collisions [11]. This corresponds to an in-medium spectral function folded over the phase-space fireball evolution up to freeze-out and appears significantly broadened (>80 MeV), so that the data should have sufficient sensitivity—in terms of mass resolution—to discriminate it. The region around the ϕ peak was fitted adding an in-medium ϕ component to the unmodified one. In the centrality integrated data, the fraction in-medium/vacuum ϕ is compatible with zero within one sigma with an upper limit of 0.08 ± 0.03 (syst) at 95% confidence level. In the two most central bins the fraction remains compatible with zero within one sigma and the upper limit increases to 0.15 ± 0.03 (syst), due the larger statistical uncertainty. The fraction predicted by Ref. [11] for semi-central data (roughly equivalent to centrality integrated data) is $\sim 4\%$. The limitation in statistics prevents us from setting a meaningful upper limit at high centrality and low p_T.

5 Conclusions and outlook

In this paper a complete characterization of $\phi \rightarrow \mu\mu$ production in In–In collisions has been provided by measuring the differential spectra, yield, mass and width.

Eur. Phys. J. C (2009) 64: 1–18

17

The rapidity distribution width does not depend on centrality within errors, and is found to be compatible with previous SPS measurements. The decay angle distributions show no evidence for polarization in any of the reference frames used, independent of centrality and p_T. This confirms the lack of anisotropy previously reported by NA60. This is a necessary though not sufficient condition for particle production from a thermalized medium. Indeed, the centrality dependence suggest that the polarization is zero or very close to zero also in peripheral collisions, close to the limit of p–p-like interactions.

The study of the transverse momentum distributions shows a small dependence of the T_{eff} parameter on the p_T window considered, to be ascribed presumably to radial flow. A blast-wave analysis shows a clear hierarchy of the freeze-out, with the ϕ being the least coupled particle to the medium. The difference between T_{eff} measured in Pb–Pb collisions by NA49 and NA50 is much larger and cannot be explained by the different p_T windows explored. The T_{eff} value for most central collisions in In–In remains significantly lower than the kaon point in Pb–Pb measured by NA49 and CERES.

The yield measured by NA50 at high p_T, when extrapolated to full p_T, exceeds the NA60 data points for the same number of participants and seems to lie outside of the general systematics. The NA60 yield, on the other hand, remains consistently larger than the NA49 and CERES Pb–Pb measurement.

The new measurements in T_{eff} and yield, when compared to the kaon channel in Pb–Pb, suggest that there may be a physical effect leading to a difference in the two channels. Further clarification may come from the NA60 measurement of the $\phi \to K^+ K^-$ channel in In–In collisions, which is currently in progress and will be reported in a forthcoming paper. At the moment, it is not possible to include all the existing SPS measurements in a coherent framework.

The mass and width were studied as a function of centrality and transverse momentum. No evidence for in-medium modifications was found. Our data were also compared to the only existing prediction for in-medium ϕ, produced in In–In collisions at 158 AGeV. The yield of such a component is compatible with zero, with an upper limit of about 8% for the centrality integrated data.

References

1. J. Rafelski, B. Muller, Phys. Rev. Lett. **48**, 1066 (1982)
2. A. Shor, Phys. Rev. Lett. **54**, 1122 (1985)
3. F. Becattini, M. Gazdzicki, J. Sollfrank, Eur. Phys. J. C **5**, 143 (1998). doi:10.1007/s100520050256, hep-ph/9710529
4. A. Andronic, P. Braun-Munzinger, K. Redlich et al., Phys. Lett. B **571**, 36 (2003)
5. F. Becattini, J. Manninen, M. Gazdzicki, Phys. Rev. C **73**, 044905 (2006)
6. F. Becattini, J. Manninen, J. Phys. G **35**, 104013 (2008)
7. B.I. Abelev et al. (STAR), Phys. Lett. B **673**, 183 (2009). doi:10.1016/j.physletb.2009.02.037, 0810.4979
8. G.E. Brown, M. Rho, Phys. Rev. Lett. **66**, 2720 (1991)
9. T. Hatsuda, S.H. Lee, Phys. Rev. C **46**, 34 (1992)
10. S. Pal, C.M. Ko, Z.-W. Lin, Nucl. Phys. A **707**, 525 (2002)
11. H. van Hees, R. Rapp, Nucl. Phys. A **806**, 339 (2008)
12. D. Cabrera, M.J. Vicente Vacas, Phys. Rev. C **67**, 045203 (2003)
13. E. Oset, A. Ramos, Nucl. Phys. A **679**, 616 (2001)
14. E.V. Shuryak, Nucl. Phys. A **661**, 119 (1999)
15. S.C. Johnson, B.V. Jacak, A. Drees, Eur. Phys. J. C **18**, 645 (2001)
16. E. Santini, G. Burau, A. Faessler et al., Eur. Phys. J. A **28**, 187 (2006)
17. R. Muto et al. (KEK-PS-E325), Phys. Rev. Lett. **98**, 042501 (2007)
18. V. Friese (NA49), Nucl. Phys. A **698**, 487 (2002)
19. C. Alt et al. (NA49), Phys. Rev. Lett. **94**, 052301 (2005)
20. S.V. Afanasev et al. (NA49), Phys. Lett. B **491**, 59 (2000)
21. B. Alessandro et al. (NA50), Phys. Lett. B **555**, 147 (2003)
22. D. Rohrich, J. Phys. G **27**, 355 (2001)
23. D. Jouan et al. (NA50), J. Phys. G **35**, 104163 (2008)
24. L. Holt, K. Haglin, J. Phys. G **31**, S245 (2005)
25. D. Adamova et al. (CERES), Phys. Rev. Lett. **96**, 152301 (2006)
26. J.R. Ellis, M. Karliner, D.E. Kharzeev et al., Phys. Lett. B **353**, 319 (1995)
27. H. Dijkstra et al. (ACCMOR), Z. Phys. C **31**, 375 (1986)
28. H. Dijkstra et al. (ACCMOR), Z. Phys. C **31**, 391 (1986)
29. R. Arnaldi et al. (NA60), Phys. Rev. Lett. **102**, 222301 (2009). nucl-ex/0812.3100
30. G. Usai et al. (NA60), Eur. Phys. J. C **43**, 415 (2005)
31. M.C. Abreu et al. (NA50), Phys. Lett. B **410**, 327 (1997). doi:10.1016/S0370-2693(97)00914-3
32. K. Banicz et al., Nucl. Instrum. Methods A **539**, 137 (2005)
33. K. Wyllie et al., in *5th Workshop on Electronics for the LHC Experiments (LEB 99)*, Snowmass, Colorado, 20–24 Sep 1999, pp. 93–97
34. J.J. van Hunen et al. (ALICE), in *7th Workshop on Electronics for LHC Experiments*, Stockholm, Sweden, 10 Sep 2001. CERN-ALI-2001-015
35. M. Keil et al., Nucl. Instrum. Methods A **546**, 448 (2005)
36. P. Rosinsky et al., Nucl. Instrum. Methods A **511**, 200 (2003)
37. V. Palmieri, K. Borer, S. Janos et al., Nucl. Instrum. Methods A **413**, 475 (1998)
38. R. Arnaldi et al., Nucl. Instrum. Methods A **411**, 1 (1998)
39. A. Colla, Ph.D. thesis, Università di Torino, 2004
40. R. Arnaldi et al. (NA60), Eur. Phys. J. C **59**, 607 (2009)
41. R. Shahoian et al. (NA60), Eur. Phys. J. C **43**, 209 (2005)
42. M. Floris, Ph.D. thesis, Università degli Studi di Cagliari, Cagliari, Italy, 2005
43. M. Floris et al. (NA60), J. Phys. Conf. Ser. **5**, 55 (2005)
44. A. David, CERN-THESIS-2006-007, 2006
45. S. Damjanovich, A. De Falco, H. Whoeri, Genesis: A hadron decay cocktail generator for the study of low mass dilepton production, 2005
46. R. Barlow, in *Advanced Statistical Techniques in Particle Physics* (2002), Grey College, Durham, 18–22 March 2002. http://www.ippp.dur.ac.uk/old/Workshops/02/statistics/proceedings//barlow.pdf
47. K. Gottfried, J.D. Jackson, Nuovo Cim. **33**, 309 (1964)
48. J.C. Collins, D.E. Soper, Phys. Rev. D **16**, 2219 (1977)
49. U.W. Heinz, hep-ph/0407360 (2004)
50. D. Teaney, J. Lauret, E.V. Shuryak, nucl-th/0110037 (2001)

18

Eur. Phys. J. C (2009) 64: 1–18

51. S. Damjanovic (NA60), J. Phys. G **35**, 104036 (2008)
52. E. Schnedermann, J. Sollfrank, U.W. Heinz, Phys. Rev. C **48**, 2462 (1993)
53. R. Arnaldi et al. (NA60), Phys. Rev. Lett. **100**, 022302 (2008)
54. G. Borges, Ph.D. thesis, Universidade Tecnica de Lisboa, Instituto Superior Tecnico, December 2005
55. C. Amsler et al. (Particle Data Group), Phys. Lett. B **667**, 1 (2008)
56. R. Arnaldi et al. (NA60), Phys. Rev. Lett. **99**, 132302 (2007)
57. E. Scomparin et al., (NA60), in *Proceedings of the 21st International Conference on Ultra-Relativistic Nucleus-Nucleus Collisions (Quark Matter 2009)*, 2009
58. C. Lourenço, NA60 Note 2007-1, http://na60.cern.ch/www/experiment/notes/2007/cc7.pdf
59. C. Alt et al. (NA49), Phys. Rev. C **73**, 044910 (2006)
60. A. De Falco et al., (NA60), in *Proceedings of the 21st International Conference on Ultra-Relativistic Nucleus-Nucleus Collisions (Quark Matter 2009)*, 2009
61. R. Arnaldi et al., Phys. Rev. Lett. **96**, 162302 (2006)
62. J. Ruppert, C. Gale, T. Renk et al., Phys. Rev. Lett. **100**, 162301 (2008)